AGU PUBLICATIONS

Geophysical Research Letters

RESEARCH LETTER
10.1002/2015GL063203

Key Points:
- Changes in sea ice and snow cover induce a negative Arctic Oscillation in winter
- An atmospheric model has deficits in reproducing the negative Arctic Oscillation
- Deficits in the simulated planetary wave propagation are identified

Supporting Information:
- Readme
- Figure S1
- Figure S2
- Figure S3

Correspondence to:
D. Handorf,
doerthe.handorf@awi.de

Citation:
Handorf, D., R. Jaiser, K. Dethloff, A. Rinke, and J. Cohen (2015), Impacts of Arctic sea ice and continental snow cover changes on atmospheric winter teleconnections, *Geophys. Res. Lett.*, *42*, 2367–2377, doi:10.1002/2015GL063203.

Received 21 JAN 2015
Accepted 28 FEB 2015
Accepted article online 4 MAR 2015
Published online 1 APR 2015

Impacts of Arctic sea ice and continental snow cover changes on atmospheric winter teleconnections

Dörthe Handorf[1], Ralf Jaiser[1], Klaus Dethloff[1], Annette Rinke[1], and Judah Cohen[2]

[1]Alfred Wegener Institute, Helmholtz Center for Polar and Marine Research, Research Unit Potsdam, Potsdam, Germany, [2]Atmospheric and Environmental Research, Inc., Lexington, Massachusetts, USA

Abstract Extreme winters in Northern Hemisphere midlatitudes in recent years have been connected to declining Arctic sea ice and continental snow cover changes in autumn following modified planetary waves in the coupled troposphere-stratosphere system. Through analyses of reanalysis data and model simulations with a state-of-the-art atmospheric general circulation model, we investigate the mechanisms between Arctic Ocean sea ice and Northern Hemisphere land snow cover changes in autumn and atmospheric teleconnections in the following winter. The observed negative Arctic Oscillation in response to sea ice cover changes is too weakly reproduced by the model. The planetary wave train structures over the Pacific and North America regions are well simulated. The strengthening and westward shift of the Siberian high-pressure system in response to sea ice and snow cover changes is underestimated compared to ERA-Interim data due to deficits in the simulated changes in planetary wave propagation characteristics.

1. Introduction

The Arctic is on the track to a new climate regime dominated by thinner first year ice [*Kwok and Rothrock*, 2009]. The decline in Arctic summer sea ice concentration is connected with atmospheric circulation responses in the following winter months [*Cohen et al.,* 2014; *Liu et al.,* 2012; *Mori et al.,* 2014; *Overland and Wang*, 2010; *Overland et al.,* 2011; *Vihma*, 2014] and linked to anomalous cold winters over Eurasia [*Honda et al.,* 2009; *Cohen et al.,* 2014] and other regions of the Northern Hemisphere [*Cohen et al.,* 2014; *Francis et al.,* 2009]. Sea ice decline leads to an enhanced absorption of solar radiation in the mixed layer of the Arctic Ocean in autumn intensifies the vertical fluxes of heat and moisture into the atmosphere. This can be seen in model results and reanalysis data [e.g., *Rinke et al.,* 2013; *Screen and Simmonds*, 2010; *Kim et al.,* 2014]. As shown by *Sato et al.* [2014], horizontal advection of heat and moisture can reduce the strength of vertical latent and sensible heat fluxes. Since there are no in situ measurements of vertical latent and sensible heat fluxes available, reliable trends in these fluxes following sea ice decline cannot be estimated as discussed by *Boisvert et al.* [2013]. Through reduced vertical stability, baroclinic systems grow in autumn and exert a strong impact on the intensification of planetary waves in the coupled troposphere-stratosphere system in the following winter [*Jaiser et al.,* 2012]. Eliassen-Palm fluxes [*Jaiser et al.,* 2012, 2013; *Trenberth*, 1986] due to planetary waves are enhanced as a result of the stronger diabatic heat source associated with the larger open ocean areas when Arctic sea ice is low. The enhanced baroclinic systems and modified cloud development processes impact the hydrological cycle and snowfall over the continental areas [*Park et al.,* 2013; *Ghatak et al.,* 2010]. Therefore, in addition to sea ice changes, associated snow cover changes affect the winter large-scale atmospheric circulation [*Cohen et al.,* 2013]. Interactions between baroclinic processes and large-scale planetary wave changes trigger a negative surface Arctic Oscillation (AO) signal that extends up to the stratosphere in winter, which is connected to reduced sea ice cover in late summer [*Kim et al.,* 2014; *Jaiser et al.,* 2013]. Another process impacting the winter AO signal is related to Siberian snow cover anomalies in October. Though the satellite data [*Robinson et al.,* 1993] exhibit a positive trend in October snow cover, *Brown and Derksen* [2013] found a negative trend using reanalysis data, in situ snow depth observations, and passive microwave data. Despite this observational uncertainty in the trend of October snow extent, positive anomalies of Siberian snow cover in October enhance planetary wave activity resulting in a negative winter AO signal [*Cohen et al.,* 2007, 2012; *Allen and Zender*, 2011]. The sea ice-related and snow cover-related mechanisms are connected through changed moisture budgets following the Arctic sea ice decline [*Cohen et al.,* 2012]. Low sea ice and extensive snow cover, by influencing the characteristics of baroclinic cyclones and

the AO pattern, modify the exchange of heat and moisture between the warmer ocean and the atmosphere [*Kim et al.,* 2014; *Cohen et al.,* 2012; *Orsolini et al.,* 2012; *Sokolova et al.,* 2007].

Here we investigate the relationships between the recent Arctic sea ice decline and snow cover changes over the continental land areas with atmospheric circulation changes on the basis of one of the most reliable reanalysis data set from 1979 to 2012 (ERA-Interim) [*Dee et al.,* 2011]. We compare the reanalysis data with ensemble simulations of the atmospheric general circulation model (AGCM) European Centre/Hamburg 6 (ECHAM6) [*Stevens et al.,* 2013] from 1979 to 2008 to check whether a state-of-the-art AGCM is able to reproduce the observed relationships. To understand the differences in the observed and simulated atmospheric circulation response in winter following sea ice and snow cover anomalies in autumn, the wave activity in the troposphere and the stratosphere has been diagnosed similar to *Jaiser et al.* [2012, 2013] and *Sokolova et al.* [2007].

2. Data and Methodology

2.1. Data and Model Simulations

We used observed monthly sea ice concentration fields from the Hadley Centre Sea Ice and Sea Surface Temperature (HadISST) data set [*Rayner et al.,* 2003; www.metoffice.gov.uk/hadobs/hadisst/], and observed monthly snow cover fields from Rutgers University snow data set [*Robinson et al.,* 1993; http://climate.rutgers.edu/measures/snowice/]. The sea ice index, defined as monthly mean sea ice extent, has been provided by the National Snow and Ice Data Center [*Fetterer and Knowles*, 2004; ftp://sidads.colorado.edu/DATASETS/NOAA/G02135/Sep/N_09_area.txt]. Based on this sea ice index for September, we defined the time period 1979–1999 as high ice phase. The time period 2000–2012 with considerably smaller mean values of sea ice extent is referred to as low ice phase. Atmospheric reanalysis data ERA-Interim have been obtained from the European Centre for Medium-Range Weather Forecasts [*Dee et al.,* 2011; http://apps.ecmwf.int/datasets/].

The ensemble simulations of the AGCM ECHAM6 [*Stevens et al.,* 2013] have been performed by the Coupled Model Intercomparison Project Phase 5 (CMIP5) project [*Taylor et al.,* 2012] as part of the CMIP5 Atmospheric Model Intercomparison Project (AMIP) simulations. The analyzed ensemble simulations are available from the CMIP5 archive (http://cmip-pcmdi.llnl.gov/cmip5/). The model simulations have been performed over the period from 1979 to 2008 with a horizontal spectral resolution of T63 (approximately 2° in longitude and latitude) and 96 vertical levels up to 0.01 hPa (about 80 km). At the lower boundary, the atmospheric model is driven by observed midmonth sea surface temperature and sea ice concentration data that is linearly interpolated to obtain daily forcing values [*Hurrell et al.,* 2008; http://www-pcmdi.llnl.gov/projects/amip/AMIP2EXPDSN/BCS/amipobs_dwnld.php]. The analyzed ensemble comprises three members. All results are described with regard to the ensemble mean for each season, year, and period, respectively.

2.2. Statistical and Dynamical Analysis

The statistical relation between fields of sea ice concentration or snow cover and atmospheric data is analyzed using a maximum covariance analysis (MCA) [*von Storch and Zwiers*, 1999]. Prior to the MCA, each field has been detrended by removing the long-term linear trend. The MCA results in pairs (MCA modes) of spatial patterns and associated time series for each field, which are coupled through a maximized covariance of their associated time series. For each MCA mode, the spatial patterns are shown as regression maps determined by regressing both data fields (sea ice concentration or snow cover and atmospheric fields) of the MCA onto the same standardized associated time series for the atmospheric field for the respective MCA mode. Therefore, the regression maps for the atmospheric fields are called homogeneous regression maps, whereas the regression maps for the sea ice concentration or snow cover fields are called heterogeneous regression maps. The regression maps represent typical anomaly patterns associated with the MCA. Statistical significance of the regression maps is determined by applying a two-tailed Student's *t* test for correlation at 95% confidence level.

The localized Eliassen-Palm fluxes (EP flux) have been computed [see *Jaiser et al.,* 2013; *Trenberth*, 1986; *Cohen et al.,* 2007] to diagnose the wave activity in the troposphere and the stratosphere. For the calculation of flux terms not influenced by the seasonal trends, the seasonal cycle has been removed. To consider the changes in synoptic-scale and planetary-scale fluxes separately, two digital filters are used [*Blackmon and Lau*, 1980]. Synoptic-scale fluctuations are extracted by a band-pass filter sensitive to time periods between

2.5 and 6 days. Periods longer than 10 days known as planetary-scale fluctuations have been filtered with a low-pass filter. Statistical significance of correlations of magnitude of EP flux vectors with sea ice and snow cover indices is assessed using a two-tailed Student's *t* test for correlation at 90% and 95% confidence level. Furthermore, differences in magnitude of EP flux vectors between the time periods are investigated for significance using a Mann-Whitney-Wilcoxon test with 90% and 95% confidence level.

3. Results and Discussions

By applying a MCA, optimized coherent large-scale patterns of September sea ice concentration and October snow cover extent have been detected, which covary with the atmospheric circulation structures in the following winter. Figure 1 displays the first pair of coupled MCA patterns of Arctic sea ice concentration in September (HadISST monthly mean data) with ERA-Interim fields of sea level pressure (SLP), 500 hPa, and 50 hPa geopotential height fields (GPH500 and GPH50) in winter (December-January-February (DJF) mean) for the period 1979–2012. The leading MCA patterns explain 44%, 32%, and 56% (for SLP, GPH500, and GPH50) of the squared covariance fraction. At all levels, the leading MCA mode describes diminishing sea ice over the northern edge of the Barents Sea, Kara, Laptev, Chukchi, and Beaufort Seas covarying with a pressure anomaly pattern resembling the negative phase of the AO throughout the troposphere and stratosphere with a predominantly zonally symmetric response. In the troposphere, this mode leads to a weakened Icelandic Low and a westward shifted and strengthened Siberian High.

There is a statistical connection between September sea ice anomalies over the Arctic and November sea ice anomalies in the Barents and Kara Seas. This sea ice decline in November could be connected with warm southerly advection induced by the poleward shift of the baroclinic zone over the Gulf Stream as stated by *Sato et al.* [2014]. As pointed out by *Jaiser et al.* [2013], the September sea ice anomaly forces a negative AO response via barotropic-baroclinic interactions, whereas the November ice anomaly directly changes the planetary wave train as suggested by *Honda et al.* [2009] and *Sato et al.* [2014]. *Jaiser et al.* [2013] prioritize the importance of vertical heat and moisture fluxes in September, whereas *Sato et al.* [2014] assume that meridional flux advection in early winter is the main trigger for the wave train changes.

The second most important pairs of coupled MCA patterns between the sea ice concentration field and atmospheric fields of SLP, GPH500, and GPH50 (Figure 2) explain 18%, 21%, and 11% of the squared covariance fraction, respectively. In the troposphere, a September sea ice pattern with seaice retreat over the Beaufort Sea and over the East Siberian Sea and northern Barents and Kara Seas is preceding a more wavelike atmospheric response. At the surface, the SLP anomaly pattern is characterized by an enhanced pressure anomaly westward of the Aleutian Low in the North Pacific and northward shift of the Icelandic Low. Over Eurasia, a positive circulation anomaly appears which again contributes to a westward shifted and strengthened Siberian High. At 500 hPa, the atmospheric anomaly pattern shows distinct similarity with the surface anomaly pattern. In the stratosphere, a wave number 1 pattern indicating a shift of the polar vortex toward Canada and Alaska is related to sea ice retreat over the Beaufort Sea and northern Kara Sea.

Figure 3 displays the leading MCA patterns of Arctic sea ice concentration in September (HadISST data) with the ECHAM6 ensemble mean fields of SLP, GPH500, and GPH50 in winter for the period 1979–2008. The MCA modes explain 38%, 37%, and 51% (for SLP, GPH500, and GPH50) of the squared covariance fraction. In the troposphere, the leading MCA patterns bear resemblance with the second MCA patterns from the reanalysis data (Figure 2). That means the September sea ice retreat over the Beaufort and the East Siberian Seas precedes an atmospheric wave train response over the Pacific and North America. Over the North Atlantic, a northward shift of the Icelandic Low is detected. The centers of action of the atmospheric patterns are stronger over the Pacific region than over the Atlantic region, and the observed westward shifted and strengthened Siberian High is not simulated. In the stratosphere, a weak wave number 1 pattern related to sea ice decline in the Laptev Sea appears with a shift of the polar vortex toward Canada. The model indicates in the second MCA mode (not shown) changes in the Siberian high-pressure system in accordance with observations connected to sea ice reduction over the Beaufort Sea and a partly reproduction of the observed negative AO pattern.

By applying an MCA to the Northern Hemisphere snow cover based on the Rutgers University snow data set for October from 1979 to 2012 [*Robinson et al.,* 1993] and the ERA-Interim SLP and GPH500 fields in winter

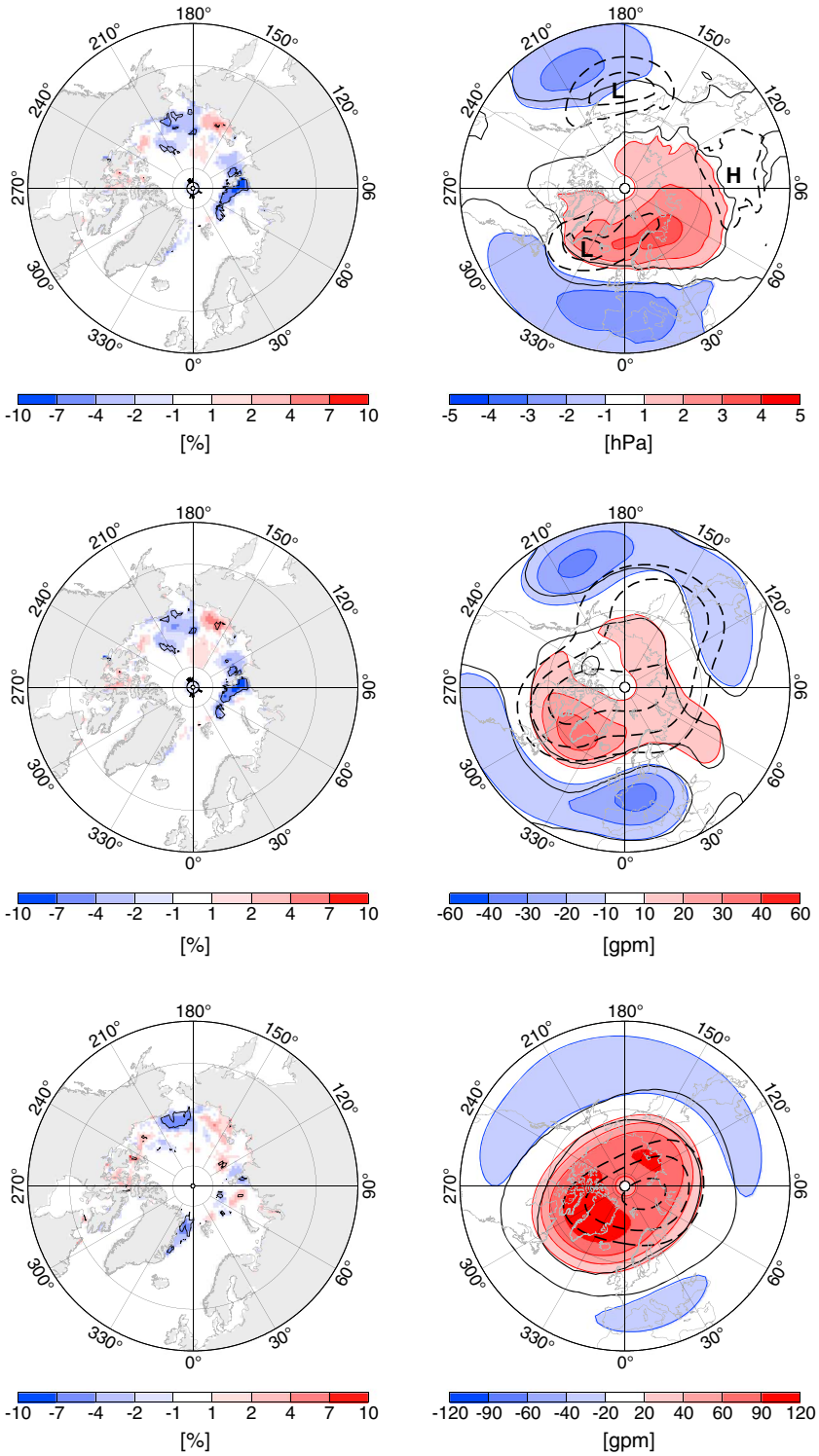

Figure 1. First pair of coupled patterns obtained by the maximum covariance analysis (MCA) of HadISST1 sea ice concentration in September with (top row) ERA-Interim sea level pressure, (middle row) GPH500 fields, and (bottom row) GPH50 fields in winter (DJF mean) from 1979 to 2012. (left column) The sea ice concentration anomaly maps (in [%]) as heterogeneous regression maps. (right column) The corresponding anomaly maps for the atmospheric variables as homogeneous regression maps. Thin black contours show the significance of the regressions at the 95% level. Dashed contours show the climatological mean (1980–2012) atmospheric fields of SLP, GPH500, and GPH50, respectively. All data have been linearly detrended before calculating the MCA.

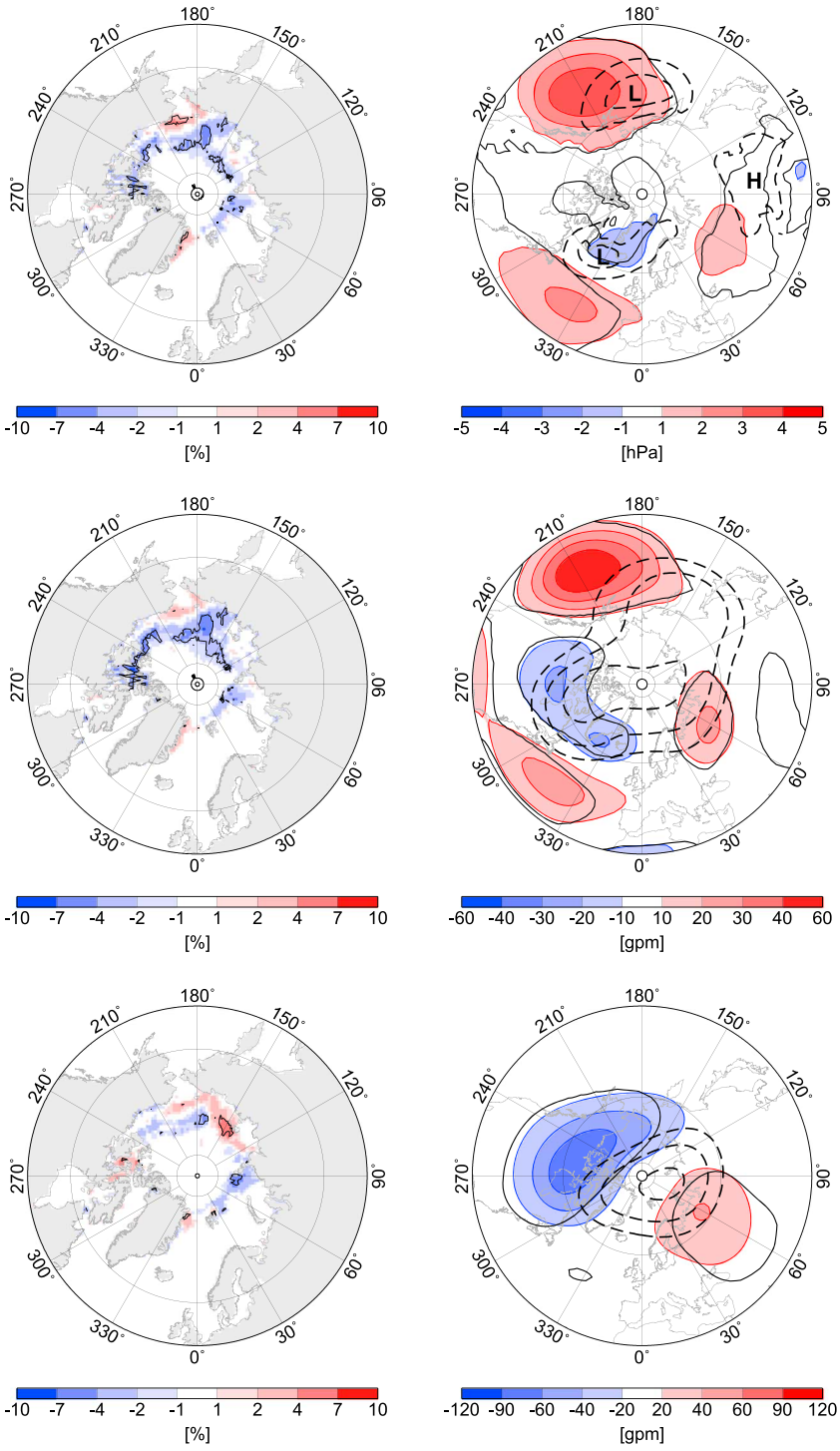

Figure 2. Second pair of coupled patterns obtained by the MCA of HadISST1 sea ice concentration in September with (top row) ERA-Interim sea level pressure, (middle row) GPH500 fields, and (bottom row) GPH50 fields in winter (DJF mean) from 1979 to 2012. (left column) The sea ice concentration anomaly maps in (in %) as heterogeneous regression maps. (right column) The corresponding anomaly maps for the atmospheric variables as heterogeneous regression maps. The black contours show the significance of the right regressions at the 95% level. Dashed contours show the climatological mean (1980–2012) atmospheric fields of SLP, GPH500, and GPH50, respectively. All data have been linearly detrended before calculating the MCA.

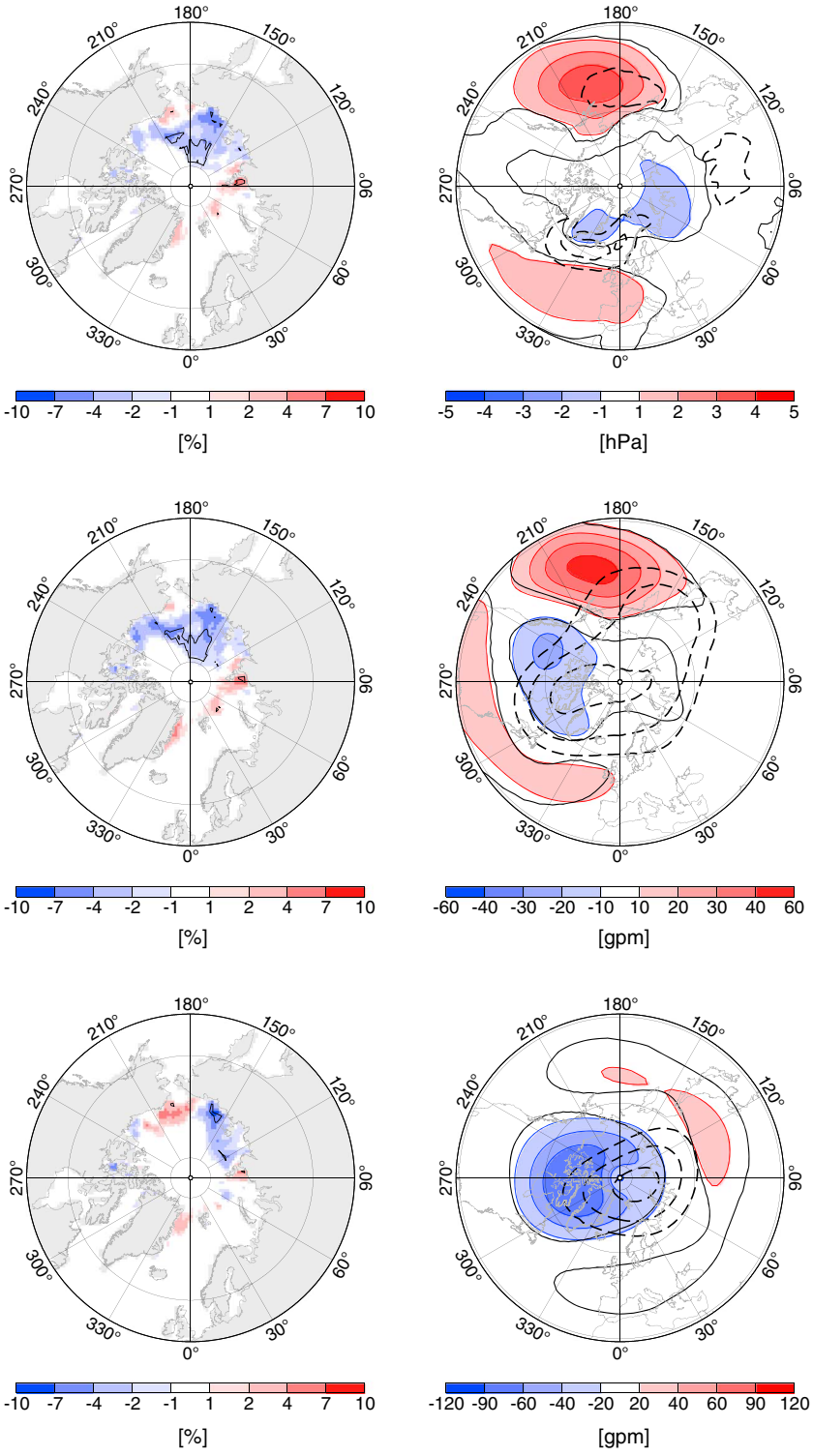

Figure 3. As in Figure 1 but for the first pair of coupled patterns obtained by MCA of HadISST1 sea ice concentration in September with (top row) ECHAM6 model-simulated sea level pressure, (middle row) GPH500 fields, and (bottom row) GPH50 fields in winter (DJF mean) from 1979 to 2008. All model data are from the ensemble mean of three ECHAM6-AMIP simulations from 1979 to 2008.

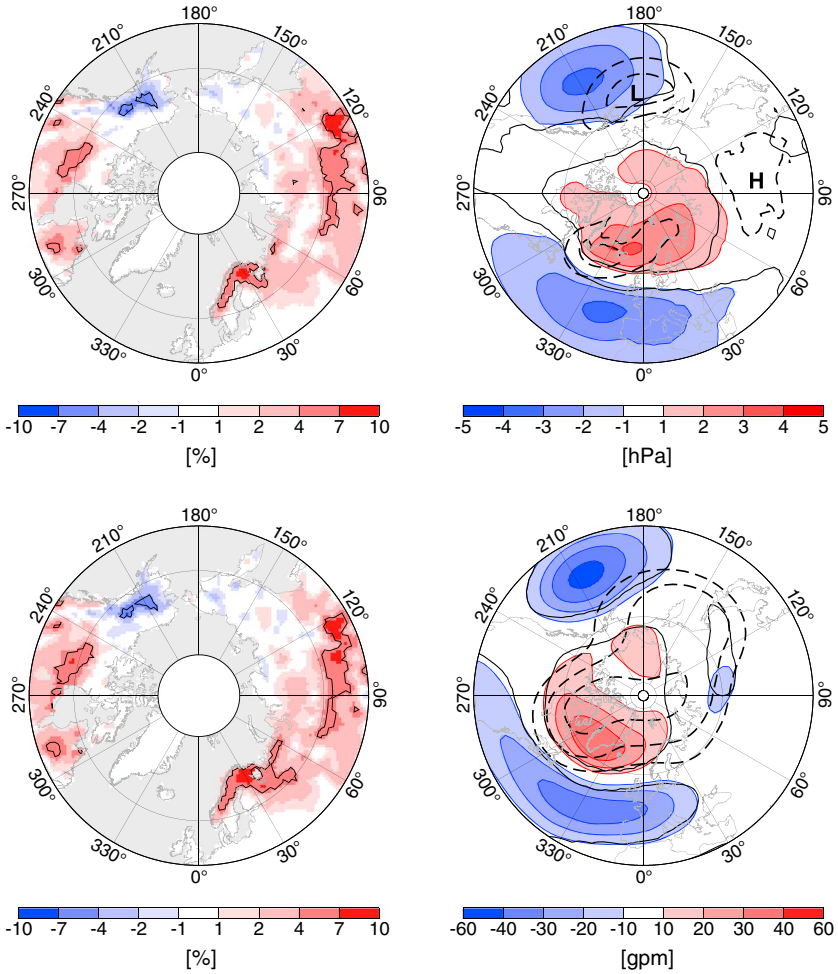

Figure 4. As in Figure 1 but for the first pair of coupled patterns obtained by MCA of October snow cover (from Rutgers University snow data set) with (top row) ERA-Interim sea level pressure and (bottom row) GPH500 in winter (DJF mean) from 1979 to 2012.

(DJF mean for the period 1979–2012), again a quasi-barotropic atmospheric response pattern with zonally symmetric character is detected and displayed in Figure 4. These coupled patterns explain 45% and 39% of the squared covariance. A pattern of enhanced snow cover over Canada, Scandinavia, northern European Russia, and the southern part of Siberia is related to pressure anomaly patterns resembling the negative phase of the AO.

As for the reanalysis data, an MCA was also applied to the fields of Northern Hemisphere snow cover distribution for October with ECHAM6 ensemble mean fields of SLP and GPH500 in winter (DJF mean). The snow cover fields have been taken as the ensemble mean of the October snow cover simulated by ECHAM6. The leading pair of MCA patterns (supporting information Figure S1) between simulated snow cover anomalies and simulated atmospheric fields of SLP and GPH500 explains 26% and 30% of the squared covariance fraction which is less than in the reanalysis data. The snow cover changes of the leading mode display increase over large parts of eastern Siberia and northwest America and decrease over west Siberia and eastern North America. The structure and amplitude of this pattern are different compared to those obtained by the MCA with the reanalysis data, which suggest differences between the simulated and observed snow cover. The related atmospheric response fields of this leading mode are characterized by quasi-barotropic wave structures and bear a strong similarity with the simulated leading atmospheric patterns related to sea ice changes (compare Figures S1 and 3).

The model underestimates the strong negative AO response to sea ice and snow cover anomalies detected in the reanalysis data. To understand the origin of these model shortcomings in the atmospheric circulation response in winter following sea ice and snow cover anomalies in autumn, the wave activity in the troposphere

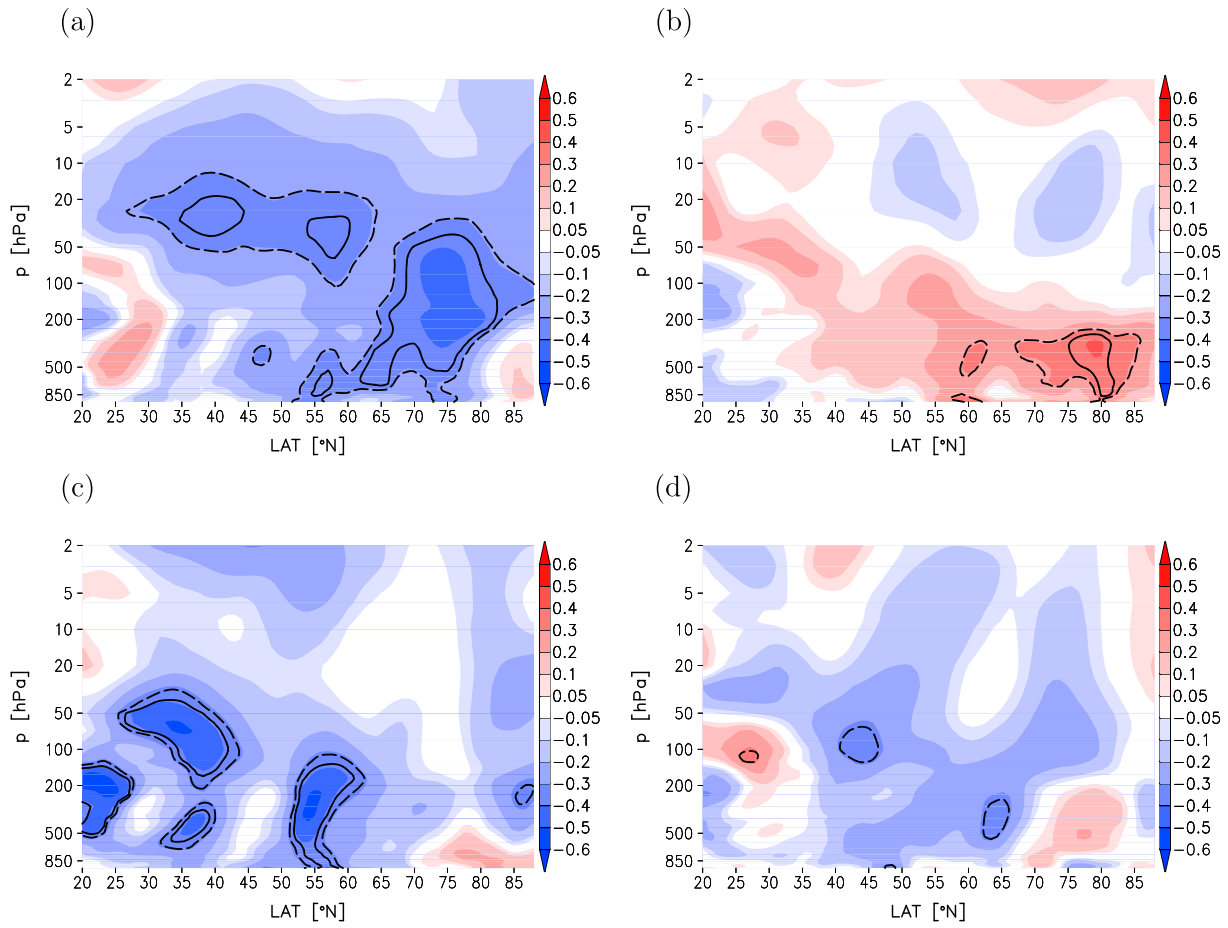

Figure 5. (a) Correlation of the zonally averaged magnitude of the planetary-scale wave EP flux vector, calculated for ERA-Interim data for winter (DJF) with preceding September sea ice index from 1979 to 2012. Statistical significance with a 90% (95%) confidence level is delineated by dashed (solid) black contour. (b) Same as in Figure 5a but for correlation of the zonally averaged magnitude of the planetary-scale wave EP flux vector, calculated for ERA-Interim data for winter (DJF) with preceding October snow cover index from 1979 to 2012 (calculated from Rutgers University snow data set). (c and d) The same as in Figures 5a and 5b but the zonally averaged magnitude of the planetary-scale wave EP flux vector and the October snow cover index for Figure 5d have been calculated for simulated data from the ensemble mean of ECHAM6-AMIP runs from 1979 to 2008.

and the stratosphere has been diagnosed [*Jaiser et al.,* 2012, 2013; *Sokolova et al.,* 2007]. The localized Eliassen-Palm (EP) flux vectors [*Trenberth*, 1986] (see section 2) have been calculated for baroclinic-scale waves (time scale of 2.5–6 days) and for planetary-scale waves (time scale of 10–90 days).

Figure 5a displays the correlation of the September sea ice index with the zonally averaged magnitude of planetary-scale EP flux vector in winter calculated from reanalysis data over the period 1979–2012. Reduced sea ice is connected with enhanced EP fluxes in the whole troposphere and lower stratosphere northward of ~50°N. The corresponding correlations between the zonally averaged magnitude of planetary-scale EP flux vector in winter with the September sea ice index for the ECHAM6 simulations over the period 1979–2008 are shown in Figure 5c. In accordance with the reanalysis data, enhanced planetary-scale EP fluxes in the troposphere and stratosphere are related to reduced sea ice, but the latitudinal belt of significant correlations is shifted to the south, and no significant signals are detected over the polar regions north of 60°N.

Similar correlation analyses have been performed for an October snow cover index (defined as area average of snow cover over 0°–190°E, 50°–90°N, based on the Rutgers University snow data set). Based on reanalysis data, the correlations between the snow cover index and the magnitude of EP fluxes are positive in the whole tropospheric polar cap connecting enhanced snow cover to increased EP fluxes (see Figure 5b). The comparison of Figures 5a and 5b gives hints on a vertically more extended impact of sea ice anomalies on the planetary wave fluxes in winter compared to the impact of snow cover anomalies. The correlations

between zonally averaged magnitudes of planetary-scale EP flux vectors in winter with the simulated October snow cover index (defined as area average of snow cover over 0°–190°E, 50°–90°N) over the period 1979–2008 for the ECHAM6 ensemble are shown in Figure 5d. In contrast to the results for the reanalysis data (Figure 5b), the model simulations do not reveal statistically significant correlations. The modeled snow cover impact is weaker relative to the observations and suggests deficits in the coupled atmosphere-snow-soil feedbacks over land which impacts on the wave propagation from the surface into the stratosphere.

The impact of tropospheric changes following variability in autumn sea ice and snow cover onto the overlying stratosphere is determined by the troposphere-stratosphere coupling and is studied in terms of the related changes in the activity and propagation of planetary-scale waves. The winter climatology (i.e., the long-term average over the winters 1979–2012) of the zonally averaged magnitude of the planetary-scale EP fluxes for the ERA-Interim data is shown in the supporting information Figures S2a and S2b separately for the Atlantic Ocean sector (average over 60°W–30°E) and the Pacific Ocean sector (average over 150°E–240°E). The maxima in the upper troposphere at about 50°N (Atlantic sector) and at about 35°N (Pacific sector) are related to the eddy-driven jets, which are located at these positions. At the tropopause level, the EP fluxes have a local minima and their magnitude increases with height throughout the lower and middle stratosphere.

The changes between low ice (2001–2012) and high ice (1979–2000) phases for the reanalysis data display large differences between the two ocean basins (supporting information Figures S2c and S2d). Over the Atlantic sector (Figure S2c), strong, significant changes of the magnitudes of the planetary-scale EP fluxes are found between 45°N and 70°N in the lower and middle troposphere, which are mainly due to an increase in the vertical component of the wave flux. Above 300 hPa, the increase in the EP flux in the midlatitudes is due to stronger southward wave fluxes. The increase in stratospheric fluxes is mainly determined by the enhanced vertical component of the wave fluxes. Over the Pacific (Figure S2d), the corresponding difference plot between low ice and high ice phases is characterized by negative values, except in the troposphere over the polar region. The negative differences of the magnitude of the planetary-scale EP fluxes in the stratosphere up to 10 hPa and in the midlatitude troposphere are mainly due to a weakening of the upward component of the wave flux.

The ECHAM6 ensemble mean climatology of the zonally averaged magnitude of the planetary-scale EP fluxes (shown in the supporting information Figures S3a and S3b) shows good agreement with the ERA-Interim results, in particular the tropospheric maxima are located at similar latitudes. Despite this agreement, the corresponding difference plots between low ice and high ice phases differ with those obtained from the reanalysis data. Over the Atlantic sector (Figure S3c), decreased vertical wave fluxes cause negative differences throughout the troposphere from 20°N to 80°N. The observed increase in the stratospheric wave fluxes (cf. Figure S2c) is only partly reproduced with differences in the location of the maximum values. Over the Pacific (Figure S3d), the difference plot between low ice and high ice phases is characterized by increased wave fluxes in the troposphere between 35°N and 70°N and in the whole stratosphere which is opposite to the ERA-Interim reanalysis results.

This comparison of the planetary-scale EP fluxes between ERA-Interim and ECHAM6 model results clearly indicates model deficits in the planetary wave propagation characteristics. In particular, the changes in the behavior of the upward propagating planetary-scale waves are of opposite sign in the midlatitude troposphere over the Atlantic Ocean sector and in the whole troposphere and stratosphere over the Pacific Ocean sector.

4. Conclusions

In accordance with previous studies, [*Cohen et al.,* 2013; *Liu et al.*, 2012; *Kim et al.,* 2014; *Overland and Wang*, 2010; *Francis et al.,* 2009; *Jaiser et al.,* 2012], the presented results support a negative Arctic Oscillation response to observed late summer sea ice and autumn snow cover changes on the basis of ERA-Interim reanalysis data. Due to the potential for improved seasonal to interannual climate predictions, an in-depth analysis of the performance of global atmospheric models regarding the response to sea ice and snow cover and of possible model deficits is required.

Here we showed that the observed negative AO in response to sea ice and snow cover changes is underestimated by the AGCM ECHAM6. The planetary wave train structures over the Pacific and North America region are well simulated, but the strengthening and westward shift of the Siberian high-pressure system is too weak compared with reanalysis data. We identified deficits in the simulated changes in

planetary wave propagation characteristics in response to sea ice and snow cover changes, which is one potential contributor to model deficiencies. The changes in the upward propagating planetary-scale waves are of opposite sign in the midlatitude troposphere over the Atlantic Ocean sector and in the whole troposphere and stratosphere over the Pacific Ocean sector. Our results suggest that improvements in the simulation of the forcing and propagation of planetary-scale waves including troposphere-stratospheric feedbacks are essential for improved seasonal, interannual, and decadal climate predictions.

Acknowledgments

We thank the data centers of the European Centre for Medium-Range Weather Forecast for providing the ERA-Interim reanalysis (http://apps.ecmwf.int/datasets), of the UK Met Office Hadley Centre for providing the HadISST data set (www.metoffice.gov.uk/hadobs/hadisst/), of the Rutgers University for providing the observed monthly snow cover fields (http://climate.rutgers.edu/measures/snowice/), and of the National Snow and Ice Data Center for providing the monthly mean sea ice extent (ftp://sidads.colorado.edu/DATASETS/NOAA/G02135/Sep/N_09_area.txt). We acknowledge the World Climate Research Programme's Working Group on Coupled Modelling, which is responsible for CMIP, and we thank in particular the climate modeling groups at Max Planck Institute for Meteorology, Hamburg, Germany, and at the German Climate Computing Center (DKRZ), Hamburg, Germany, for producing and making available their model output. For CMIP, the U.S. Department of Energy's Program for Climate Model Diagnosis and Intercomparison provides coordinating support and led development of software infrastructure in partnership with the Global Organization for Earth System Science Portals. We are particularly grateful to Sabine Erxleben for her support in conducting data analysis and preparing the figures.

The Editor thanks Timo Vihma and an anonymous reviewer for their assistance in evaluating this paper.

References

Allen, R. J., and C. S. Zender (2011), Forcing of the Arctic oscillation by Eurasian snow cover, *J. Clim.*, *24*, 6528–6539, doi:10.1175/2011JCLI4157.1.

Blackmon, M. L., and N.-C. Lau (1980), Regional characteristics of the Northern Hemisphere wintertime circulation: A comparison of the simulation of a GFDL general circulation model with observations, *J. Atmos. Sci.*, *37*, 497–514, doi:10.1175/1520-0469(1980)037<0497:RCOTNH>2.0.CO;2.

Boisvert, L., T. Markus, and T. Vihma (2013), Moisture flux changes and trends for the entire Arctic in 2003–2011 derived from EOS Aqua data, *J. Geophys. Res. Oceans*, *118*, 5829–5843, doi:10.1002/jgrc.20414.

Brown, R. D., and C. Derksen (2013), Is Eurasian October snow cover extent increasing?, *Environ. Res. Lett.*, *8*, 024006, doi:10.1088/1748-9326/8/2/024006.

Cohen, J., M. Barlow, P. J. Kushner, and K. Saito (2007), Stratosphere-troposphere coupling and links with Eurasian surface variability, *J. Clim.*, *20*, 5335–5343, doi:10.1175/2007JCLI1725.1.

Cohen, J., J. Furtado, J. M. Barlow, V. Alexeev, and J. Cherry (2012), Arctic warming, increasing snow cover and widespread boreal winter cooling, *Environ. Res. Lett.*, *7*, 014007, doi:10.1088/1748-9326/7/1/014007.

Cohen, J., J. Jones, J. C. Furtado, and E. Tziperman (2013), Warm Arctic, cold continents: A common pattern related to Arctic sea ice melt, snow advance, and extreme winter weather, *Polar Oceanogr.*, *26*, 152–160.

Cohen, J., et al. (2014), Recent Arctic amplification and extreme mid-latitude weather, *Nat. Geosci.*, *7*, 627–637, doi:10.1038/ngeo2234.

Dee, D. P., et al. (2011), The ERA-Interim reanalysis: Configuration and performance of the data assimilation system, *Q. J. R. Meteorol. Soc.*, *137*, 553–597, doi:10.1002/qj.828.

Fetterer, F., and K. Knowles (2004), Sea ice index monitors polar ice extent, *Eos Trans. AGU*, *85*, 163, doi:10.1029/2004EO160007.

Francis, J. A., W. Chan, D. J. Leathers, J. R. Miller, and D. E. Veron (2009), Winter Northern Hemisphere weather patterns remember summer Arctic sea-ice extent, *Geophys. Res. Lett.*, *36*, L07503, doi:10.1029/2009GL037274.

Ghatak, D., A. Frei, G. Gong, J. Stroeve, and J. Robinson (2010), On the emergence of an Arctic amplification signal in terrestrial Arctic snow extent, *J. Geophys. Res.*, *115*, D24105, doi:10.1029/2010JD014007.

Honda, M., J. Inoue, and S. Yamane (2009), Influence of low Arctic sea-ice minima on anomalously cold Eurasian winters, *Geophys. Res. Lett.*, *36*, L08707, doi:10.1029/2008GL037079.

Hurrell, J. W., J. J. Hack, D. Shea, J. M. Caron, and J. A. Rosinski (2008), A new surface temperature and sea ice boundary dataset for the community atmosphere model, *J. Clim.*, *21*, 5145–5153, doi:10.1175/2008JCLI2292.1.

Jaiser, R., K. Dethloff, D. Handorf, A. Rinke, and J. Cohen (2012), Planetary- and synoptic-scale feedbacks between tropospheric and sea ice cover changes in the Arctic, *Tellus, Ser. A*, *64*, 11595, doi:10.3402/tellusa.v64i0.11595.

Jaiser, R., K. Dethloff, and D. Handorf (2013), Stratospheric response to Arctic sea ice retreat and associated planetary wave propagation changes, *Tellus, Ser. A*, *65*, 19375, doi:10.3402/tellusa.v65i0.19375.

Kim, B. M., S. W. Son, S. K. Min, J. H. Jeong, S. J. Kim, X. Zhang, T. Shim, and J. H. Yoon (2014), Weakening of the stratospheric polar vortex by Arctic sea-ice loss, *Nat. Commun.*, *5*, 4646, doi:10.1038/ncomms5646.

Kwok, R., and D. A. Rothrock (2009), Decline in Arctic sea ice thickness from submarine and ICESat records: 1958–2008, *Geophys. Res. Lett.*, *36*, L15501, doi:10.1029/2009GL039035.

Liu, J., J. A. Curry, H. Wang, M. Song, and R. Horton (2012), Impact of declining Arctic sea ice on winter snowfall, *Proc. Natl. Acad. Sci. U.S.A.*, *109*, 4074–4079, doi:10.1073/pnas.1114910109.

Mori, M., M. Watanabe, H. Shiogama, J. Inoue, and M. Kimoto (2014), Robust Arctic sea-ice influence on the frequent Eurasian cold winters in past decades, *Nat. Geosci.*, *7*, 869–873, doi:10.1038/NGEO2277.

Orsolini, Y., R. Senan, R. Benestad, and A. Melsom (2012), Autumn atmospheric response to the 2007 low Arctic sea ice extent in coupled ocean–atmosphere hindcasts, *Clim. Dyn.*, *38*, 2437–2448, doi:10.1007/s00382-011-1169-z.

Overland, J. E., and M. Wang (2010), Large-scale atmospheric circulation changes are associated with the recent loss of Arctic sea ice, *Tellus, Ser. A*, *62*, 1–9, doi:10.1111/j.1600-0870.2009.00421.x.

Overland, J. E., K. R. Wood, and M. Wang (2011), Warm Arctic—Cold continents: Impacts of the newly open Arctic Sea, *Polar Res.*, *30*, 15787, doi:10.3402/polar.v30i0.15787.

Park, H., J. E. Walsh, Y. Kim, T. Nakai, and T. Ohata (2013), The role of declining Arctic sea ice in recent decreasing terrestrial Arctic snow depths, *Polar Sci.*, *7*, 174–187, doi:10.1016/j.polar.2012.10.002.

Rayner, N. A., D. E. Parker, E. B. Horton, C. K. Folland, L. V. Alexander, D. P. Rowell, E. C. Kent, and A. Kaplan (2003), Global analyses of sea surface temperature, sea ice, and night marine air temperature since the late nineteenth century, *J. Geophys. Res.*, *108*(D14), 4407, doi:10.1029/2002JD002670.

Rinke, A., K. Dethloff, W. Dorn, D. Handorf, and J. C. Moore (2013), Simulated Arctic atmospheric feedbacks associated with late summer sea ice anomalies, *J. Geophys. Res. Atmos.*, *118*, 7698–7714, doi:10.1002/jgrd.50584.

Robinson, D. A., K. F. Dewey, and R. R. Heim (1993), Global snow cover monitoring: An update, *Bull. Am. Meteorol. Soc.*, *74*, 1689–1696, doi:10.1175/1520-0477(1993)074<1689:GSCMAU>2.0.CO;2.

Sato, K., J. Inoue, and M. Watanabe (2014), Influence of the Gulf Stream on the Barents Sea ice retreat and Eurasian coldness during early winter, *Environ. Res. Lett.*, *9*, 084009, doi:10.1088/1748-9326/9/8/084009.

Screen, J. A., and I. Simmonds (2010), Increasing fall-winter energy loss from the Arctic Ocean and its role in Arctic temperature amplification, *Geophys. Res. Lett.*, *37*, L16707, doi:10.1029/2010GL044136.

Sokolova, E., K. Dethloff, A. Rinke, and A. Benkel (2007), Planetary and synoptic scale adjustment of the Arctic atmosphere to sea ice cover changes, *Geophys. Res. Lett.*, *34*, L17816, doi:10.1029/2007GL030218.

Stevens, B., et al. (2013), Atmospheric component of the MPI-M Earth system model: ECHAM6, *J. Adv. Model. Earth Syst.*, *5*, 146–172, doi:10.1002/jame.20015.

Taylor, K. E., R. J. Stouffer, and G. A. Meehl (2012), An overview of CMIP5 and the experiment design, *Bull. Am. Meteorol. Soc.*, *93*, 485–498, doi:10.1175/BAMS-D-11-00094.1.

Trenberth, K. E. (1986), An assessment of the impact of transient eddies on the zonal flow during a blocking episode using localized Eliassen-Palm flux diagnostics, *J. Atmos. Sci.*, *43*, 2070–2087, doi:10.1175/1520-0469(1986)043<2070:AAOTIO>2.0.CO;2.

Vihma, T. (2014), Effects of Arctic sea ice decline on weather and climate: A review, *Surv. Geophys.*, *35*, 1175–1214, doi:10.1007/s10712-014-9284-0.

von Storch, H., and F. W. Zwiers (1999), *Statistical Analysis in Climate Research*, 494 pp., Cambridge Univ. Press, Cambridge, U. K.